Three-dimensional deformation caused by the Bam, Iran, earthquake and the origin of shallow slip deficit

Yuri Fialko[1], David Sandwell[1], Mark Simons[2], Paul Rosen[3]

[1]*Institute of Geophysics and Planetary Physics, Scripps Institution of Oceanography, University of California San Diego, La Jolla, CA*

[2]*Seismological Laboratory, Division of Geological and Planetary Sciences, California Institute of Technology, Pasadena, CA*

[3]*Jet Propulsion Laboratory, California Institute of Technology, Pasadena, CA*

We derive the full vector displacement field due to the M_w6.5 Bam (Iran) earthquake using radar data from the Envisat satellite of the European Space Agency. Analysis of surface deformation indicates that most of the seismic moment release along the 20-km-long strike-slip rupture occurred at a shallow (4-5 km) depth, yet the rupture did not break the surface. The Bam event is therefore an end-member case of a shallow slip deficit model postulating that the coseismic slip in the uppermost crust is systematically less than that at the seismogenic depth (4-10 km). The InSAR-derived surface displacement data from the Bam and other large shallow earthquakes suggest that the uppermost section of the seismogenic crust around young and developing faults may undergo a distributed failure (thereby accumulating little elastic strain) in the interseismic period.

Introduction

Understanding of the earthquake process requires detailed insights into how the tectonic stresses are accumulated and released on seismogenic faults. Over the last decade, new information about the near-field deformation due to several large shallow earthquakes was

obtained with the help of the space-borne Synthetic Aperture Radar (SAR) measurements [1–3]. Interpretations of the spatially continuous SAR data from the best documented seismic events including the M_w7.3 Landers[4], the M_w7.6 Izmit[5,6], and the M_w7.1 Hector Mine [3,7,8] earthquakes all reveal the maximum seismic moment release in the middle of the seismogenic layer (the average depth of 4-6 km). While a gradual decay in the coseismic slip at the bottom of the seismogenic layer is likely compensated by postseismic and interseismic strain accumulation, and is reasonably well understood[9–11], the apparent discrepancy between slip in the middle and shallow parts of the seismogenic layer remains enigmatic. The uppermost few kilometers of the brittle crust are known to have different mechanical properties compared to the rest of the upper crust. In particular, the shallow layer has a higher density of cracks, pores, and voids[12], a higher coefficient of friction[13], and may exhibit velocity-strengthening behavior[14]. While the latter may explain why the coseismic slip may be impeded in the shallow crust, it is not clear how the resulting deficit of shallow slip is accommodated throughout the earthquake cycle. Steady state shallow creep has been inferred from the SAR data in some localities (e.g., on the southern section of the San Andreas fault [15]), but more often has not been observed. The remaining alternatives are episodic shallow creep, shallow postseismic afterslip, or a distributed inelastic failure of the shallow crust, either during earthquakes[3], or in the interseismic period. The mechanisms of accumulation and release of stress and strain in the shallow seismogenic crust are of interest because most of the seismic and geodetic measurements of deformation are done at the surface or in shallow boreholes. The mode of deformation and the state of stress in the uppermost crust are also important for predictions of the intensity of ground shaking, and the associated seismic hazards in the vicinity of large seismogenic faults. In this paper we report on deformation associated with the M_w6.5 Bam (Iran) earthquake determined using the Synthetic Aperture Radar data from the ERS and Envisat satellites of the European Space Agency. The Bam earthquake is the first large ($M_w > 6$) shallow earthquake for which the decorrelation of the radar images does not prevent measurements of surface displacements across the earthquake

rupture, thereby allowing robust insights into the problem of the shallow slip deficit.

The $M_w 6.5$ Bam earthquake occurred on December 26, 2003, in south-east Iran within a diffuse boundary between the Arabian and Eurasian plates. It was one of the deadliest earthquakes in the region's history, with estimated several tens of thousands casualties. The earthquake rupture occurred directly below the town of Bam (Figure S1), causing a nearly complete destruction of old un-reinforced (predominantly mudbrick), as well as modern buildings. Teleseismic (USGS and Harvard CMT) and preliminary aftershock data[16] indicate a strike-slip mechanism with a right-lateral slip on a nearly vertical fault. The epicentral area of the earthquake was imaged by the ASAR (advanced SAR) instrument on board of the Envisat satellite within several weeks of the seismic event, with acquisitions available from the ascending and descending satellite orbits. Table 1 lists the radar acquisitions used in this study. We generated four independent projections of the coseismic displacement field using differences in the radar phase[17] and the radar amplitude[8,18] before and after the earthquake from both the ascending and descending orbits (see Methods section). The radar line of sight (LOS) displacements and the pixel offsets along the satellite tracks are shown in Figures 1a,b and 1c,d, respectively. The strike-slip mechanism and the north-south orientation of the Bam rupture are optimal in that they maximize the azimuthal pixel offsets (AZO). The correlation of the radar images is exceptionally good, presumably due to arid conditions and sparse vegetation. The only decorrelated areas around the northern end of the rupture are due to a massive destruction (and, possibly, postearthquake rescue and remedy activities) in the town of Bam.

3-D coseismic offsets due to the Bam earthquake

We combine the four projections of surface deformation (Figures 1a-d) to deduce the full 3-D vector displacement filed due to the Bam earthquake[4,8]. Figures 1e and 1f show the vertical and horizontal components of the coseismic deformation, respectively. The data pairs from the ascending and descending orbits include several weeks of possible postseismic relaxation.

The latter is likely negligible compared to the coseismic offsets, as evidenced by observations of postseismic deformation due to large strike-slip earthquakes elsewhere[19–21]. Therefore it is reasonable to believe that the data shown in Figure 1 are dominated by the coseismic deformation.

The location of the earthquake rupture is readily identifiable in the horizontal displacement map as the north-south striking plane of symmetry between the butterfly-shaped lobes of the coseismic offsets (Figures 1f). Such a spatial pattern, as well as the antisymmetry of both the horizontal and vertical displacements with respect to the fault plane, is predicted by elastic dislocation models of the earthquake source[4,8,22]. The coseismic displacement field inferred from the Envisat ASAR data reveals somewhat greater displacement amplitudes on the eastern side of the fault, implying either a contrast in the elastic moduli between the eastern and western sides of the fault, or a small eastward deviation of the fault plane from vertical. To determine the sub-surface fault structure we inverted the interferometric and the azimuthal offset data (Figures 1a-d) for the fault geometry and slip distribution (see Methods section). Figure S2 shows the slip model that best explains the ASAR data, and Figure S3 of the supplemental materials shows the model predictions and the data residuals. The best-fitting model indicates predominantly right-lateral displacements having a maximum amplitude of about 2 meters at depth of 3 to 7 km. The geodetic moment determined by summation of the dislocation potencies (area times slip), and multiplying the sum by the typical value of the shear modulus of the Earth crust (30 GPa) is of the order of $6\text{-}8\times10^{18}$ N m. This corresponds to the moment magnitude of 6.5-6.6, in excellent agreement with the seismically determined values[16]. A major peculiarity of the inferred slip model is that the maximum moment release occurred at a fairly small depth ($\sim$4 km), yet the slip did not reached the surface (Figure S2). The lack of surface rupture due to the Bam earthquake is evidenced by the continuity of fringes in the radar interferograms (Figures 1a-b), and is confirmed by field investigations[16,23]. Figure 2 shows the absolute value of horizontal displacements from a 4-km wide swath across the central part of the Bam rupture (see Figure

4

1f). One can see from Figure 2 that the surface offsets on the surface trace of the Bam rupture do not exceed a few centimeters, and are much smaller than the maximum horizontal displacements of 0.5-0.6 m that occur at a distance of about 1.5 km away from the rupture trace. Small-to-moderate ($M_w < 6$) crustal earthquakes typically do not break the surface because they nucleate at depth, and have a characteristic rupture size that is small compared to the thickness of the brittle layer[24,25]. This is not the case for the Bam rupture, which has a characteristic horizontal dimension of about 20 kilometers (Figures S1 and S2), i.e. sufficient to saturate the entire upper crust.

Nature of the shallow slip deficit

Given that the crustal strength decreases toward the surface[13,26], the termination of slip in the uppermost crust indicates either significant velocity strengthening or negligible preseismic elastic strain at depths above 2-3 kilometers (or a combination of the above). Qualitatively, the distribution of slip due to the Bam earthquake is similar to those inferred for other large strike-slip earthquakes for which high quality geodetic data are available. Figure 3 shows the average seismic potency per unit length of rupture for the Bam (this study), Landers[4], Izmit[6], and Hector Mine[3] earthquakes. In all cases, the maximum release of seismic moment occurs in the middle of the brittle layer, and decreases toward the surface[27]. Assuming that the earthquake rupture is an ergodic process (i.e., global spatial sampling is equivalent to local temporal sampling over many earthquake cycles), results shown in Figure 3 pose a dilemma: either the elastic dislocation models are inadequate for interpretation of the coseismic deformation data, or much of the stress release in the shallow crust occurs aseismically. The former hypothesis implies that the observed inflection (i.e., change in sign of the second spatial derivative), or even non-monotonic behavior (change in sign of the first spatial derivative, as is the case for the Bam earthquake) of the surface displacements in the near field of the seismic rupture is due to an essentially inelastic response of the uppermost few kilometers of the brittle crust[3]. In this case, the shallow slip deficit is an

artifact of inverse models that are based on elastic solutions[28,29], and the surface slip need not to be systematically less than the maximum slip at depth. Unfortunately, the surface displacements inferred from previous SAR studies cannot be directly compared to the fault offsets measured in the field because of the decorrelation of the radar images around the earthquake rupture[3,4,6,8]. The data from the Bam earthquake are unambiguous in that the displacements can be continuously traced across the fault, indicating no slip in the shallow crust (Figures 1, 2, and S2). The data shown in Figures 1f and 2 indicate that the assumption of no co-seismic slip deficit implies that the inelastic deformation in the shallow crust is distributed within a $\sim$3 km wide shear zone. This implication is not supported by inspections of the radar phase coherence in the earthquake epicentral area, which show a rather localized zone of surface damage having width of the order of tens to hundreds of meters, and field observations of microcracking and small-scale offsets limited to the rupture trace of the fault[23].

Regardless of whether the coseismic slip in the top few kilometers of the seismogenic layer is inhibited by the velocity strengthening behavior, or low shear stress, the observed slip deficit apparently has to be accommodated aseismically, as intermediate-size earthquakes as well as microseismicity in the top 2-3 km of the crust are extremely rare. It has been proposed that the coseismically induced stress changes may give rise to an accelerated stable slip in the shallow velocity strengthening layer[30]. While a significant shallow afterslip has been documented on faults that are prone to creep in the interseismic period[31,32], more often it has not been observed[6,19–21]. Our analysis of InSAR data over the time period of 2 months following the Bam earthquake also does not reveal any shallow afterslip on the earthquake rupture (Figure 2). Preliminary InSAR results spanning a time period of 10 months after the earthquake confirm that the slip deficit was not relieved in the postseismic period.

Previous studies have shown that some shallow slip may be triggered on faults as a result of nearby earthquakes[8,34,35]. However, the amount of such triggered slip (integrated over the earthquake cycle) is unlikely to account for the estimated slip deficit of the order

6

of meters. Another possibility is that the localized shallow slip occurs at a nearly constant rate during the interseismic period. Some faults are inferred to undergo a quasi-steady state shallow creep[15,26,33]. However, decade-long InSAR observations in the Eastern California Shear Zone[21,36] and other seismically active areas around the world suggest that the steady shallow creep is an exception rather than a rule, especially for immature and infrequently slipping faults such as the Bam rupture. Analysis of the ERS SAR data spanning the time period between 1992 and 1999 lends further support to this conclusion (see Figure 2 and Table 1).

We propose that the shallow slip deficit results from a distributed inelastic deformation within the uppermost few kilometers of the Earth's crust, occurring predominantly during the interseismic period. The non-brittle long-term behavior of the uppermost crust is well known from field studies of compressional tectonics (in particular, blind thrust faults)[37,38]. For strike-slip faults, the intersesimic deformation may involve a predominantly elastic deformation of the upper crust below ~2-3 km, and predominantly inelastic deformation of the uppermost layer due to folding, granular flow, or some other distributed failure mechanism. Alternatively, the uppermost crust may be partially decoupled from the seismogenic layer, for example, by a low friction interface. In both cases the infrequently slipping strike-slip faults that rarely break the surface may be very difficult to detect from geologic and paleoseismologic observations[23]. The non-localized nature of near-surface deformation is consistent with velocity-strengthening friction and low absolute strength of the poorly consolidated uppermost crust[26], and may explain the "flower structures" associated with major strike-slip faults[39,40]. According to our hypothesis the shallow crust can be either weak or strong (e.g., able to support stresses predicted by the Byerlee's law), but may not accumulate significant elastic strain due to the slow tectonic loading. At the same time, it might deform elastically on short time scales (corresponding, e.g., to the coseismic deformation), as evidenced by the coseismic response of large compliant fault zones[4,41]. Whether or not the earthquake rupture reaches the surface may be controlled by the amount of the earthquake stress drop in

the velocity-weakening part of the crust, and the level of the preseismic stress in the shallow layer. If the shallow layer is weak, the upward rupture propagation from the seismogenic part of the crust may give rise to a dynamic overshoot in the shallow layer. The ongoing drilling experiment on the San Andreas fault[42] will presumably penetrate the transition between the velocity-strengthening and velocity-weakening layers within the seismogenic crust, and provide direct observational constraints on the level of stresses at which the upper sections of major strike-slip faults operate. Note that the data presented in this paper characterize deformation due to relatively young or infrequently slipping faults with small cumulative offsets. It remains to be seen whether the shallow slip deficit is typical of mature faults capable of great (magnitude larger than 8) earthquakes. A good agreement between the geologic and present day geodetic slip rates on the central section of the San Andreas fault[43] may be indicative of high localization of strain throughout the earthquake cycle. In contrast, geologically inferred slip rates on relatively young and developing faults are often systematically less than the geodetic estimates[44], consistent with our interpretation.

A distributed failure of the near-surface layer due to the secular tectonic loading implies that estimates of the depth of the brittle-ductile transition from geodetic measurements of the interseismic strain accumulation on major crustal faults may be systematically underestimated by an amount equivalent to the thickness of the anelastic surface layer. The particular modes of deformation of the shallow crust have important implications for the seismic energy release and the intensity of ground shaking in epicentral areas of moderate-to-large crustal earthquakes. Because the uppermost crust may store little density of the potential energy of elastic deformation, it is not likely to participate in the elastic rebound, which might compound the effects of the velocity strengthening in dampening of the seismic energy radiation. This implies smaller velocities and accelerations at the Earth's surface (compared to the ideal elastic-brittle behavior of the entire upper crust), and, consequently, reduced potential damage due to shallow earthquakes.

References

[1] Massonnet, D. *et al.* The displacement field of the Landers earthquake mapped by radar interferometry. *Nature* **364**, 138–142 (1993).

[2] Peltzer, G., Crampe, F. & King, G. Evidence of nonlinear elasticity of the crust from the $M_w7.6$ Manyi (Tibet) earthquake. *Science* **286**, 272–276 (1998).

[3] Simons, M., Fialko, Y. & Rivera, L. Coseismic deformation from the 1999 $M_w7.1$ Hector Mine, California, earthquake, as inferred from InSAR and GPS observations. *Bull. Seism. Soc. Am.* **92**, 1390–1402 (2002).

[4] Fialko, Y. Probing the mechanical properties of seismically active crust with space geodesy: Study of the co-seismic deformation due to the 1992 $M_w7.3$ Landers (southern California) earthquake. *J. Geophys. Res.* **109**, 10.1029/2003JB002756 (2004).

[5] Feigl, K.L. *et al.* Estimating slip distribution for the Izmit mainshock from coseismic GPS, ERS-1, RADARSAT and SPOT measurements. *Bull. Seism. Soc. Am.* **92**, 138–160 (2002).

[6] Cakir, Z. *et al.* Coseismic and early post-seismic slip associated with the 1999 Izmit earthquake (Turkey), from SAR interferometry and tectonic field observations. *Geophys. J. Int.* **155**, 93–93 (2003).

[7] Jonsson, S., Zebker, H., Segall, P. & Amelung, F. Fault slip distribution of the 1999 M_w 7.1 Hector Mine, California, earthquake, estimated from satellite radar and GPS measurements. *Bull. Seism. Soc. Am.* **92**, 1377–1389 (2002).

[8] Fialko, Y., Simons, M. & Agnew, D. The complete (3-D) surface displacement field in the epicentral area of the 1999 $M_w7.1$ Hector Mine earthquake, southern California, from space geodetic observations. *Geophys. Res. Lett.* **28**, 3063–3066 (2001).

[9] Tse, S. T. & Rice, J. R. Crustal earthquake instability in relation to the depth variation of frictional slip properties. *J. Geophys. Res.* **91**, 9452–9472 (1986).

[10] Thatcher, W. Nonlinear strain build-up and the earthquake cycle on the San Andreas fault. *J. Geophys. Res.* **88**, 5893–5902 (1983).

[11] Savage, J. & Svarc, J. Postseismic deformation associated with the 1992 M_w=7.3 Landers earthquake, southern California. *J. Geophys. Res.* **102**, 7565–7577 (1997).

[12] Manning, C. & Ingebritsen, S. Permeability of the continental crust: Implications of geothermal data and metamorphic systems. *Rev. Geophys.* **37**, 127–150 (1999).

[13] Byerlee, J. Friction of rock. *Pure Appl. Geophys.* **116**, 615–626 (1978).

[14] Marone, C. Laboratory-derived friction laws and their application to seismic faulting. *Annu. Rev. Earth Planet. Sci.* **26**, 643–696 (1998).

[15] Lyons, S. & Sandwell, D. Fault creep along the southern San Andreas from interferometric synthetic aperture radar, permanent scatterers, and stacking. *J. Geophys. Res.* **108**, 10:1029/2002JB001831 (2003).

[16] Report of the International Institute of Earthquake Engineering and seismology, `http://www.iiees.ac.ir/English/Bam_report_english.html`.

[17] Rosen, P. *et al.* Synthetic aperture radar interferometry. *Proc. of the IEEE* **88**, 333–382 (2000).

[18] Michel, R. & Avouac, J.-P. Measuring ground displacements from SAR amplitude images: Application to the Landers earthquake. *Geophys. Res. Lett.* **26**, 875–878 (1999).

[19] Peltzer, G., Rosen, P., Rogez, F. & Hudnut, K. Poroelastic rebound along the Landers 1992 earthquake surface rupture. *J. Geophys. Res.* **103**, 30131–30145 (1998).

[20] Jacobs, A., Sandwell, D., Fialko, Y. & Sichoix, L. The 1999 (M_w7.1) Hector Mine, California, earthquake: Near-field postseismic deformation from ERS interferometry. *Bull. Seism. Soc. Am.* **92**, 1433–1442 (2002).

[21] Fialko, Y. Evidence of fluid-filled upper crust from observations of post-seismic deformation due to the 1992 M_w7.3 Landers earthquake. *J. Geophys. Res.* **109**, 10.1029/2004JB002985 (2004).

[22] Chinnery, M. A. The deformation of the ground around surface faults. *Bull. Seism. Soc. Am.* **51**, 355–372 (1961).

[23] Talebian, M. *et al.* The 2003 Bam (Iran) earthquake: Rupture of a blind strike-slip fault. *Geophys. Res. Lett.* **31**, L11611, doi:10.1029/2004GL020058 (2004).

[24] Heaton, T. Evidence for and implications of self-healing pulses of slip in earthquake rupture. *Phys. Earth Planet. Inter.* **64**, 1–20 (1990).

[25] Boatwright, J. Spectral theory for circular seismic sources - simple estimates of source dimension, dynamic stress drop, and radiated seismic energy. *Bull. Seism. Soc. Am.* **70**, 1–27 (1980).

[26] Savage, J. & Lisowski, M. Inferred depth of creep on the Hayward fault, central California. *J. Geophys. Res.* **98**, 787–793 (1993).

[27] The near-surface decrease in the coseismic slip may be less apparent for the Izmit earthquake because of the low resolution of both the available slip models and the data (due to significant decorrelation of the ground around the earthquake rupture). Other finite source models of the Izmit earthquake show a more pronounced slip deficit[5,45].

[28] Okada, Y. Surface deformation due to shear and tensile faults in a half-space. *Bull. Seismol. Soc. Am.* **75**, 1135–1154 (1985).

[29] Wang, R., Martin, F. & Roth, F. Computation of deformation induced by earthquakes in a multi-layered elastic crust - FORTRAN programs EDGRN/EDCMP. *Comp. Geosci.* **29**, 195–207 (2003).

[30] Marone, C., Scholz, C. & Bilham, R. On the mechanics of earthquake afterslip. *J. Geophys. Res.* **96**, 8441–8452 (1991).

[31] Williams, P., McGill, S., Sieh, K., Allen, C. & Louie, J. Triggered slip along the San-Andreas fault after the 8 July 1986 North Palm-Springs earthquake. *Bull. Seism. Soc. Am.* **78**, 1112–1122 (1988).

[32] Bilham, R. Surface slip subsequent to the 24 November 1987 Superstition Hills, California, earthquake monitored by digital creepmeters. *Bull. Seism. Soc. Am.* **79**, 424–450 (1989).

[33] Bürgmann, R. *et al.* Earthquake potential along the northern Hayward fault, California. *Science* **289**, 1178–1182 (2000).

[34] Sandwell, D., Sichoix, L., Agnew, D., Bock, Y. & Minster, J.-B. Near real-time radar interferometry of the M_w 7.1 Hector Mine Earthquake. *Geophys. Res. Lett.* **27**, 3101–3104 (2000).

[35] Sharp, R., Rymer, M. & Lienkaemper, J. Surface displacement on the Imperial and Superstition Hills faults triggered by the Westmoreland, California, earthquake of 26 April 1981. *Bull. Seism. Soc. Am.* **76**, 949–965 (1986).

[36] Peltzer, G., Crampe, F., Hensley, S. & Rosen, P. Transient strain accumulation and fault interaction in the Eastern California shear zone. *Geology* **29**, 975–978 (2001).

[37] Lettis, W., Wells, D. & Baldwin, J. Empirical observations regarding reverse earthquakes, blind thrust faults, and quaternary deformation: Are blind thrust faults truly blind? *Bull. Seism. Soc. Am.* **87**, 1171–1198 (1997).

[38] Dolan, J., Christofferson, S. & Shaw, J. Recognition of paleoearthquakes on the Puente Hills blind thrust fault, California. *Science* **300**, 115–118 (2003).

[39] Sylvester, A. Strike-slip faults. *Geol. Soc. Am. Bull.* **100**, 1666–1703 (1988).

[40] Ben-Zion, Y. *et al.* A shallow fault-zone structure illuminated by trapped waves in the Karadere-Duzce branch of the North Anatolian Fault, western Turkey. *Geophys. J. Int.* **152**, 699–699 (2003).

[41] Fialko, Y. *et al.* Deformation on nearby faults induced by the 1999 Hector Mine earthquake. *Science* **297**, 1858–1862 (2002).

[42] Hickman, S. & Zoback, M. Stress orientations and magnitudes in the SAFOD pilot hole *Geophys. Res. Lett.* **31**, Art. No. L15S12 (2004).

[43] Sieh, K. E. & Jahns, R. H. Holocene activity of the San Andreas fault at Wallace Creek, California. *Geol. Soc. Am. Bull.* **95**, 883–896 (1984).

[44] Oskin, M. & Iriondo, A. Large-magnitude transient strain accumulation on the Blackwater fault, Eastern California shear zone. *Geology* **32**, 313–316 (2004).

[45] Delouis, B., Giardini, D., Lundgren, P. & Salichon, J. Joint inversion of InSAR, GPS, teleseismic, and strong-motion data for the spatial and temporal distribution of earthquake slip: Application to the 1999 Izmit mainshock. *Bull. Seism. Soc. Am.* **92**, 278–299 (2002).

[46] Rosen, P., Hensley, S., Peltzer, G. & Simons, M. Updated repeat orbit interferometry package released. *Eos* **85**, 47 (2003).

[47] Scharoo, R. & Visser, P. Precise orbit determination and gravity field improvement for the ERS satellites. *J. Geophys. Res.* **103**, 8113–8127 (1998).

[48] Farr, T. & Kobrick, M. Shuttle Radar Topography Mission produces a wealth of data. *AGU Eos* **81**, 583–585 (2000).

[49] Tatar, M. *et al.* Aftershocks study of the 26 December 2003 Bam earthquake. *J. Seis. Earthquake Eng.* (2004). in press.

[50] Peltzer, G., Rosen, P., Rogez, F. & Hudnut, K. Postseismic rebound in fault step-overs caused by pore fluid flow. *Science* **273**, 1202–1204 (1996).

Methods: Data processing and analysis

The raw SAR data were processed using the JPL/Caltech software ROI_PAC[46], and precise satellite orbits from Delft University (Netherlands)[47]. Effects of topography were removed from the interferograms using a digital elevation model produced by the Space Shuttle Radar Topography Mission[48].

The choice of the data pairs was stipulated, in particular, by (i) optimal baselines and (ii) temporal proximity of the postearthquake acquisitions from the ascending and descending orbits (see Table 1). The small interferometric baselines of the data pairs used in this study result in much better correlation of the radar images compared to the shorter time span, but larger baseline pairs[23].

A joint inversion of the interferometric and the azimuthal offset data (Figures 1a-d) was used to infer the earthquake fault location and slip distribution. For a given fault geometry, the slip distribution was found using the least square minimization with the non-negativity constraint on the strike-slip component of the displacement vector; no sign constraints were

imposed on the dip-slip component. The optimal model smoothness was determined by investigating a trade-off between the model misfit and the degree of smoothing. The fault geometry was found using multiple slip inversions and a grid search through the model parameters defining the fault location and orientation[3,4]. The best-fitting fault geometry indicates that the earthquake rupture is steeply (5° off vertical) dipping to the East (Figure S2), which likely explains the inferred asymmetry in the surface displacement field (Figures 1 and 2).

Pair number	Acquisition dates	Orbit	$B_\perp$, m	Sensor
Coseismic				
IP1	2003/12/03-2004/02/11	Descending	2	Envisat
IP2	2003/11/16-2004/01/25	Ascending	30	Envisat
Postseismic				
IP3	2004/01/25-2004/02/29	Ascending	34	Envisat
Preseismic				
IP4	1992/12/06-1996/04/02	Descending	118	ERS-1
IP5	1992/07/19-1996/04/03	Descending	83	ERS-1,2
IP6	1993/09/12-1996/05/08	Descending	44	ERS-1,2
IP7	1992/11/01-1996/05/07	Descending	26	ERS-1
IP8	1992/07/19-1996/04/02	Descending	38	ERS-1
IP9	1992/07/19-1997/05/28	Descending	7	ERS-1,2
IP10	1993/09/12-1998/09/30	Descending	9	ERS-1,2
IP11	1996/04/02-1999/03/24	Descending	14	ERS-1,2
IP12	1996/05/07-1999/06/02	Descending	11	ERS-1,2

Table 1: The coseismic interferometric pairs used in this study. $B_\perp$ is the across-track separation between the repeated satellite orbits.

Figures

Please note: Figure numbers that correspond to those referenced in the main text are given in parentheses.
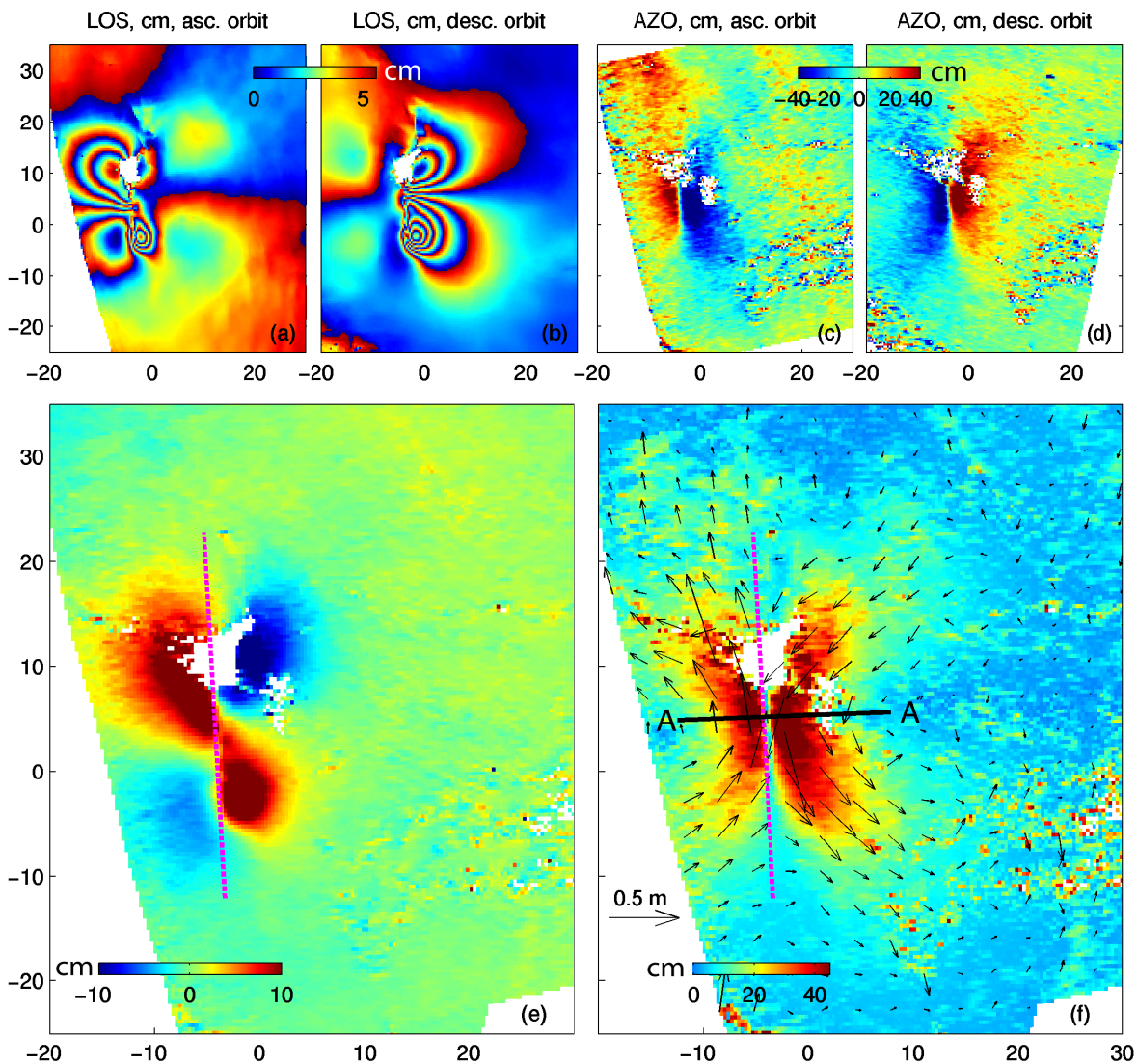
Figure 1: (1) Coseismic deformation due to the Bam earthquake as imaged by the Envisat ASAR data. The coordinate axes are in km, with the origin at 58.4°E, 29°N. Colors denote displacements in cm. (a) Interferogram for the time period November 16, 2003 - January 25, 2004, ascending orbit. (b) Interferogram for the time period December 3, 2003 - February 11, 2004, descending orbit. (c) Azimuthal offsets, ascending orbit. (d) Azimuthal offsets, descending orbit. (e) Vertical and (f) horizontal components of the surface displacement field derived from the ASAR data (Figures a-d). Arrows show the sub-sampled horizontal displacements. Dashed line shows the surface projection of the fault plane inferred from the inverse modeling of the ASAR data.

17

Figure 2: (2) Displacements along a profile A-A′ perpendicular to the Bam earthquake rupture (Figure 1). Black triangles denote the absolute value of coseismic displacements (left axis), red dots denote the postseismic LOS displacements that occurred over a time period of one to two months after the earthquake, and blue dots denote the preseismic LOS displacements that occurred over a time period between 1992 and 1999 (right axis). Red vertical line denotes the position of the rupture trace deduced from the phase correlation map. Grey bar marks a 3 km-wide zone between the maxima in the amplitude of horizontal displacements on both sides of the fault.
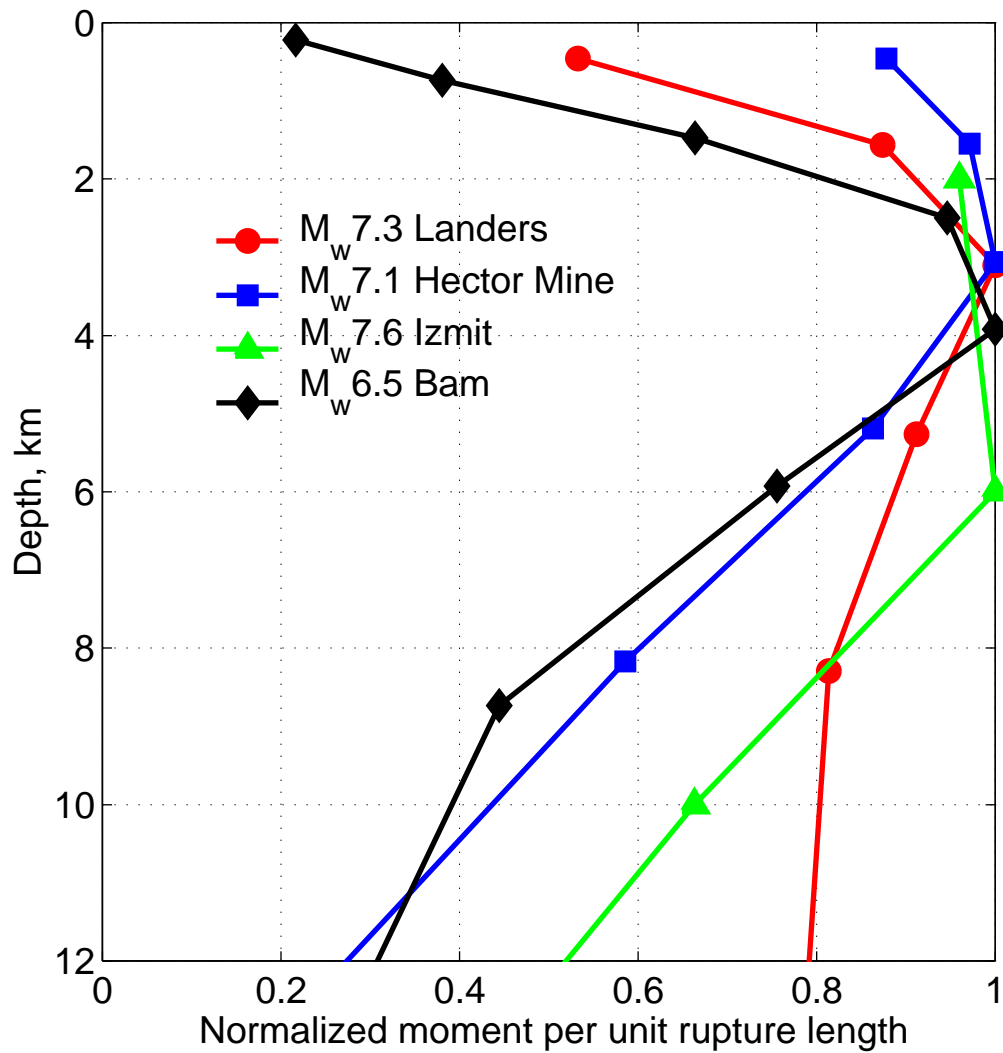
Figure 3: (3) Distribution of seismic potency $\bar{P}$ averaged along the fault length L, $\bar{P}(z) = \int_0^L P(x,z)dx / \max(\int_0^L P(x,z)dx)$, as a function of depth z, for several large strike-slip earthquakes.
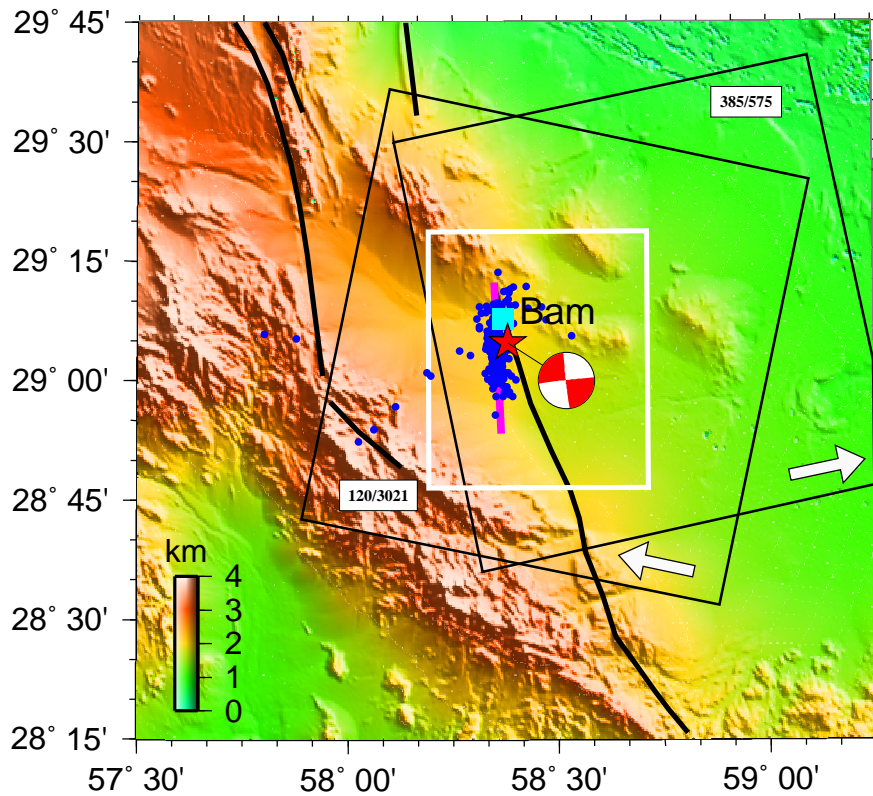
Figure 4: (S1) Shaded relief map of the epicentral area of the Bam earthquake. The earthquake epicenter is shown by a red star. The magenta line denotes the surface projection of the fault plane inferred from modeling of the surface displacement data. Black curvy lines show the geologically mapped faults. Blue square denotes the town of Bam. Blue circles denote the aftershocks[49]. Black frames and white arrows show the radar swathes and look directions, respectively. White box outlines the area shown in Figure 1.
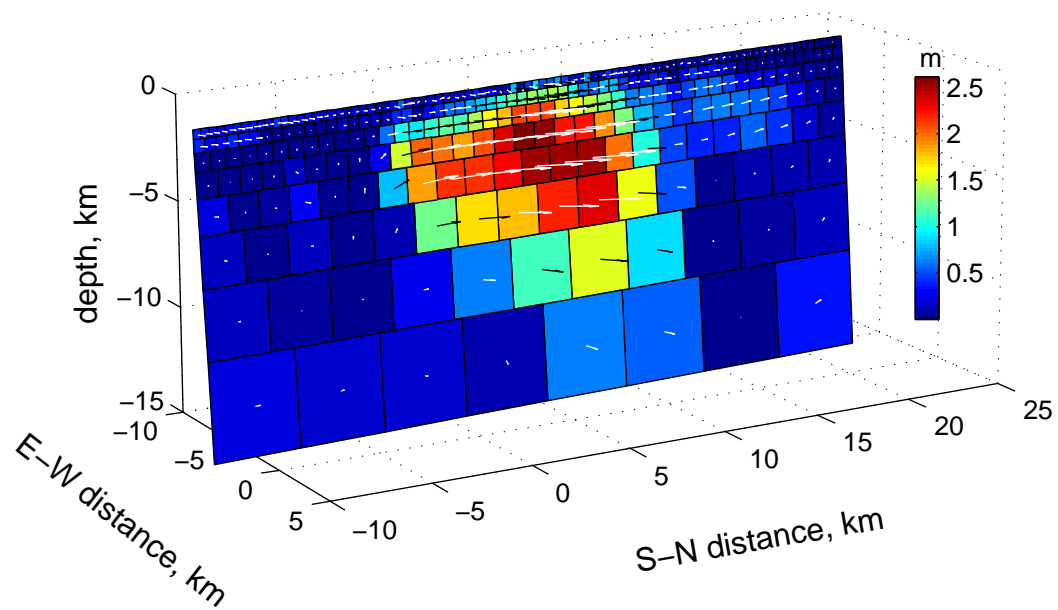
Figure 5: (S2) Slip distribution from the inversion of the Envisat ASAR data for the layered elastic half-space model. Variations of the elastic moduli with depth was inferred from the 1-D seismic velocity model[49]. Colors denote the amplitude of the strike-slip displacements, in meters, and arrows show the direction of slip on the fault plane.
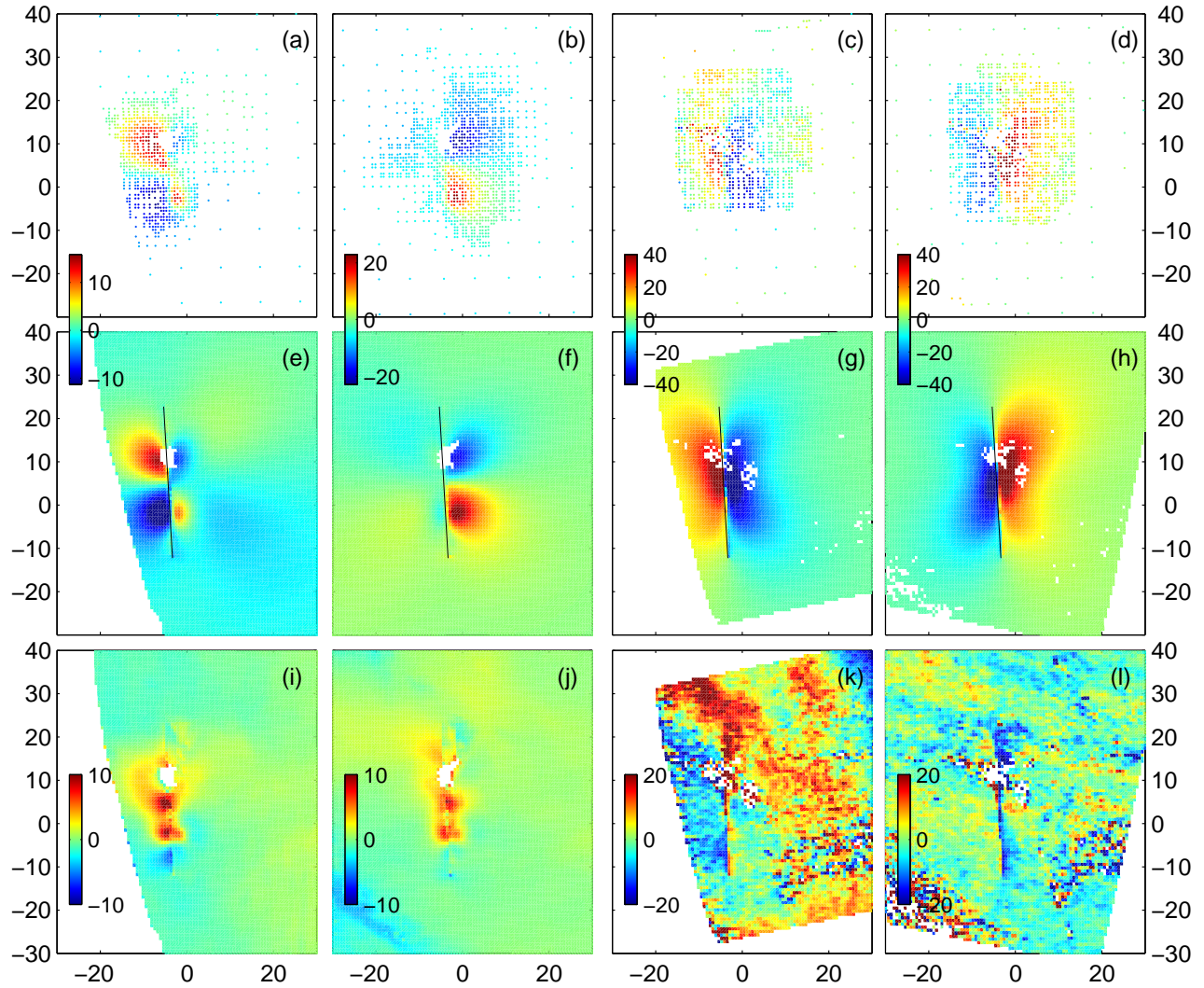
Figure 6: (S3)
(a)-(d) Sub-sampled ASAR data used in the inversion (sub-sampled data also span the rest of the radar images not shown in the figures). (e)-(h) Best-fitting models. (i)-(l) Residuals after subtracting the best-fitting models from the data. Colors denote the displacement amplitude, in centimeters. The LOS displacement residuals of the order of a few centimeters along the fault plane might be due to either co- or postseismic sources of shallow dilation [20,50].